Interdecadal Variations in the Alaska Gyre

GARY S. E. LAGERLOEF*

Science Applications International Corporation, Bellevue, Washington

(Manuscript received 28 September 1994, in final form 10 February 1995)

ABSTRACT

Climatic dynamic topography variations in the Alaska gyre during the period 1968–1990 are described with an objective analysis of more than 12 000 STD and XBT stations, and COADS wind stress data. Interannual dynamic height and SST variations were correlated and were consistent with recently described large-scale climatic shifts in the North Pacific. The gyre was centered more to the east, circulation appeared stronger, and SST was lower during the early to mid-1970s than during the 1980s. The Aleutian low (NP and PNA indices) intensified during the interim, but the response did not appear as a gyre spinup. Instead, the associated wind stress anomalies forced a slowly varying dynamic height anomaly across the eastern and northern part of the gyre through Ekman convergence, which had the effect of displacing the gyre's low somewhat to the WSW in the 1980s. The wind curl spectrum was white, and the slow oceanic response was modeled as stochastic-forced climate variability with a simple first-order Markov autoregression process. Forcing was assumed to be Ekman pumping of the pycnocline, and the damping coefficient was estimated from the data to be $\sim 1\ \mathrm{yr}^{-1}$. A hindcast with observed winds gave estimated dynamic height patterns similar to those observed, with a canonical correlation of 0.79 at 99% confidence. This response was weak in the western half of the gyre, where slow baroclinic variability may have been influenced by long Rossby wave propagation. A simple autoregression simulation using artificial white noise forcing shows the evolution of decadal variations similar in nature to those observed. This result, along with the low frequency correlation between dynamic height and SST, suggests that the upper-ocean climatic variability in this region is primarily wind forced.

1. Introduction

Oceanic variability on decadal (sub-ENSO) timescales can influence weather, fishery resources, other socioeconomic factors, and obscure climate trends, which many believe are the consequence of anthropogenic influence on the environment. Wunsch (1992) argued that interdecadal oceanic variability exists as a natural outcome of the interactions between turbulent fluids such as the ocean and atmosphere, but noted that the present oceanographic database is generally inadequate for a reliable description or understanding. There has been progress, such as in the comparatively data-rich North Atlantic, where Levitus (1989) documented large-scale middepth circulation changes between decades. However, this was based on the difference between pentadal averages and did not offer clues on the variability timescales such as could be obtained with a continuous time series. Sea surface temperature (SST) is the most extensively observed oceanic variable for climate analysis. Although encumbered with calibration problems earlier in the record, these data have been applied by numerous authors in correlation studies to assess the effect of SST anomalies on the atmosphere and vice versa (Kushnir 1994, to cite a recent example).

SST is strongly influenced by air–sea interaction and thus is not the best indicator of ocean circulation variations. Dynamic topography is more appropriate. Spaceborne altimetry is expected to accumulate long continuous global records suitable for climate studies in the future (Koblinsky et al. 1992). In the meantime, it is possible to generate dynamic topography analyses in regions relatively densely sampled by STD and XBT observations. This study applies such an analysis to the Alaska gyre, where interdecadal SST variations have been documented and a limited number of conventional oceanographic surveys have shown significant transport variations in the major currents (see below). A large XBT data resource exists, and an analysis is presented here of the available hydrographic stations spanning the years 1968 through mid-1990; 77% XBTs and 23% STD/Nansen stations (see the appendix). From these, a 22.5 year long horizontally gridded field of 0–450 decibar (dbar) dynamic height has been computed. (1 dbar $= 10^4$ Pa). The focus here is to examine gyre-scale dynamic topography variations during recent dec-

* Current affiliation: Earth and Space Research, Seattle, Washington.

Corresponding author address: Dr. Gary S. E. Lagerloef, Earth and Space Research, 10533 Ravenna Ave., NE, Seattle, WA 98125. E-mail: lagerloef@esr.org

ades, the relation to climate indices, and the dynamics of wind forcing.

Of particular interest is the low-frequency oceanic response to high-frequency wind forcing. The problem lends itself to application of stochastic forcing models (Hasselmann 1977), which can be evaluated with extensive dynamic height and wind measurements. The latter consist of monthly wind stress fields from Coupled Ocean–Atmosphere Data Set (COADS). It is evident in these data and other studies of model winds (Chave et al. 1991; Large et al. 1991) that the wind curl spectrum is white and the forcing appears stochastic (section 5). Hasselmann (1977) introduced the notion that slow climatic variability can be explained as the integral response to continuous random short-term impulses. A large frequency separation between forcing and response is an essential element of this theory. Statistically stationary climate variability is maintained with linear damping feedback and the problem expressed as a simple first-order Markov process. The theory has been applied to explain SST variability in response to random air–sea fluxes (Frankignoul and Hasselmann 1977; Frankignoul 1981; Frankignoul and Reynolds 1983). The Markov model is explored here to explain large-scale dynamic height variations as the response to stochastic vertical pycnocline displacement driven by Ekman pumping. Reed (1984) suggested time-integrated Ekman pumping might explain observed transport variations in the eastern Alaska Gyre between 1980 and 1981. Other studies of stochastic wind forcing have focused on the mesoscale response, including remote forcing, using more sophisticated models (Frankignoul and Müller 1979; Müller and Frankignoul 1981; Treguier and Hua 1987; Brink 1989; Samelson 1989, 1990; Cummins 1991; Large et al. 1991; Cummins and Freeland 1993). Here, the data duration and spatial extent allow the climatic response at lower frequencies and wavenumbers to be explored. Frankignoul and Müller (1979) showed that long Rossby wave resonance is possible at periods longer than the minimum Rossby wave period ($T_{\min} \sim 1.9$ years at 55° latitude and internal radius $L_D \sim 16$ km). Thus, we can anticipate a slow oceanic response to the low frequency and wavenumber modes in the atmosphere.

For the present application, the Markov model is expressed as

$$\frac{\partial \eta}{\partial t} = -\alpha W_E - \lambda \eta, \qquad (1)$$

where η is the dynamic height, W_E the stochastic Ekman pumping velocity, α a scaling coefficient, and λ the damping or feedback coefficient. Here $\lambda > 0$ induces a negative growth tendency to a positive anomaly and vice versa; λ has units of inverse time, and it is often convenient to express it in terms of a damping timescale λ^{-1}. At this point we will defer discussion on what physical processes play this role, as for example the atmospheric feedback proposed for stochastically forced SST anomalies by Frankignoul and Hasselmann (1977). The important features of the two-time-scale climate system can be addressed independently of the details of the upper-ocean model (Frankignoul and Hasselmann 1977), and it is only necessary to accept that some negative feedback mechanism exists. To test this model, the observed fields η and W_E were used to empirically estimate the coefficients α and λ at each grid point. These exhibit spatial patterns indicating that the wind-forced response was not uniform. The Markov model is then used with these coefficients to hindcast dynamic height from the observed winds. This hindcast field shows very good agreement with the observed field in both temporal and spatial pattern (section 5).

2. Regional ocean circulation and climate variability

The Alaska gyre is a subpolar cyclonic circulation in the northeast Pacific (Fig. 1) associated with the Aleutian low, the large-scale winter low pressure system centered over the Aleutian Islands, some 2000 km westward. The primary currents consist of a broad eastern boundary current flowing north, condensing into a narrow western boundary flow in the apex of the gyre and proceeding WSW along the Aleutian Peninsula as the Alaskan Stream. Geostrophic transports relative to 1500 dbar in the Alaskan Stream are nominally about 12–18 Sv (Sv $\equiv 10^6$ m^3 s^{-1}) (Musgrave et al. 1992). Transports as small as 2 Sv and as large as 20 Sv have been observed from intermittent surveys (Reed et al., 1980; Royer 1981). Reed et al. (1980) and Musgrave

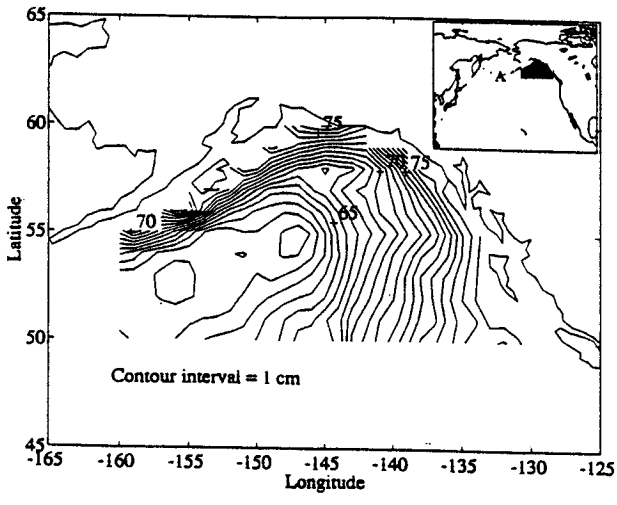

FIG. 1. Mean 0–450 dbar dynamic topography in the Alaska gyre as computed in this analysis (the appendix). Inset: the study area location (shaded) in the northeast Pacific. The letter "A" denotes the approximate mean center of the wintertime Aleutian low of surface atmospheric pressure.

et al. (1992) found that this variability was uncorrelated with seasonal Sverdrup transport estimated from integrated wind stress curl. Reed (1984) speculated that vertical pycnocline displacements, associated with shifting patterns of wind stress curl, induced east–west lateral displacements of the northward transport feeding the gyre. The importance of local wind stress curl forcing to episodic ventilation of the upper pycnocline was suggested by Van Scoy et al. (1991). Apparent lateral displacements were also evident in the early charts of Dodimead (1963). Royer and Emery (1987) suggested that these could be associated with meridional shifts in the North Pacific drift interacting barotropically with bottom topography. Musgrave et al. (1992) argue that the apparent transport variations may be an artifact of undersampling the field in the presence of large eddies. The Geosat altimeter provided high resolution sampling from 1986 to 1989. Kelly et al. (1993) described a principal mode with a large-scale sea level increase across the NE part of the gyre. Bhaskaran et al. (1993) found modes of interannual variation that correlate to climate indices such as the North Pacific pressure index (NP) and Southern Oscillation index (SOI).

SST variations of 1–3 decades duration have been identified in the gyre by Royer (1989). Correlation with Alaskan coastal air temperature records allowed extrapolation back to ~1900, wherein the period appears to have modulated from as short as 9 to as long as 23 years, and a nominal value of 16 years. The quasi-cyclic behavior has led to speculation of a link to harmonic astronomical forcing with the 18.6 year nodal tide, wherein weak meridional barotropic currents in the presence of the mean SST gradient could induce SST fluctuations on the order of 2°C (Royer 1993). In light of this, it is instructive to examine alternative processes to determine whether these SST variations are related to large-scale variations in the gyre circulation and the atmospheric forcing rather than very low frequency tides. Figure 2a shows the SST time series (2-year running mean) from the 5° latitude/longitude box in the east-central part of the gyre (centered at 55°N, 140°W, after Royer 1989). Superimposed is the first empirical orthogonal function (EOF) of the gyre dynamic height from the present study (see section 4 for details). It is immediately apparent that these indices share similar variations on interannual to interdecadal timescales (correlation $r = .74$), suggesting that SST is closely linked to the dynamic height field and related processes governing the gyre circulation.

Trenberth and Hurrell (1994) and Miller et al. (1994) describe the climatic shift in the North Pacific, which was manifested rather abruptly in the mid-1970s and persisted for about the next decade. The symptoms included deepening of the Aleutian low sea level pressure (SLP), southward displacement of Pacific storm tracks, lower SST, and deeper mixed layer across the central North Pacific and higher SST along the North

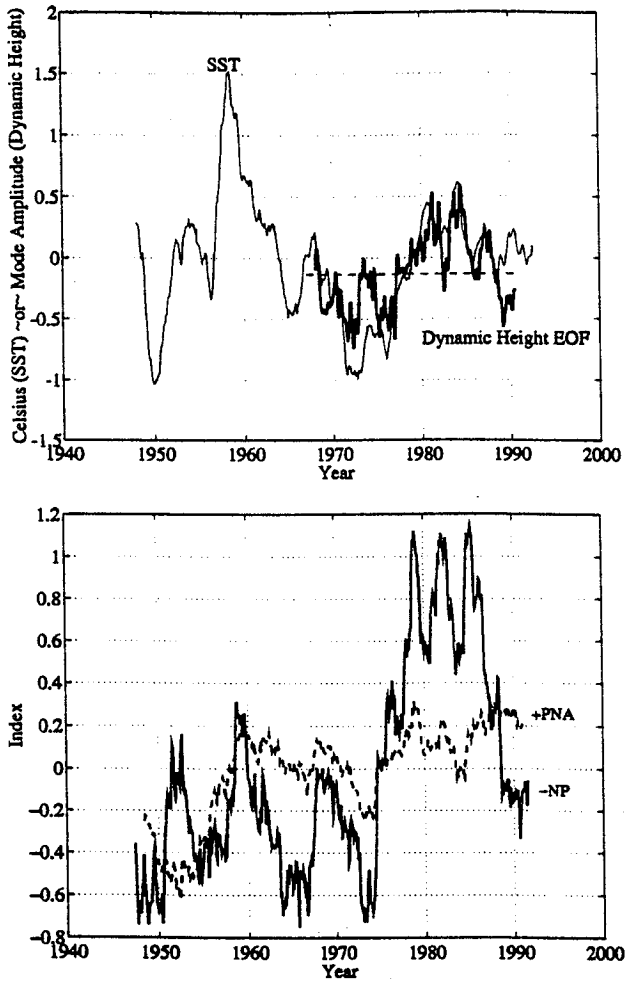

FIG. 2. (a) Light line: Time series of monthly SST anomaly in the 5° × 5° square centered at 55°N, 140°W, with a two-year running mean filter applied (monthly 5° × 5° SST data courtesy of D. Cayan, Scripps Institution of Oceanography). Dark line: Superimposed time series of the first dynamic height EOF from the present analysis. The similarity suggests that both indices reflect similar oceanic response on decadal timescales. The horizontal dashed line is the offset for the SST mean during the time interval from 1968 to 1990 and serves as the abscissa for the dynamic height EOF curve. (b) Solid line: The NP index (Trenberth and Hurrel 1994) shown negative. Dashed line: The PNA index (Wallace and Gutzler 1981). Both are 5-year running mean monthly anomalies and indicate minima in the early to mid-1970s and increase during the 1980s. An increase as plotted signifies deepening of the Aleutian low. [The signal is more robust in the NP, which is an area-average surface pressure index than the PNA, which is an upper air pressure teleconnection index. (Data courtesy of K. Trenberth, NCAR and M. Wallace, University of Washington).]

American coast and Alaska, along with changes in a host of other indices. The Pacific North America (PNA) mode (Wallace and Gutzler 1981) and the North Pacific (NP) index (Trenberth and Hurrell 1994) show trends indicating a deepening Aleutian low over the decades of the 1970s and 1980s (Fig. 2b). Trenberth (1990) showed that the 1970s climate transition

was associated with warm surface temperature anomalies over Alaska and cooler SST in the central North Pacific. Wallace et al. (1990) noted that the first EOF North Pacific SST pattern is robust, having been evident in several previous studies using various analysis techniques, domains, and periods. The pattern reflects an elongated region dominating the central North Pacific, with a reversal of sign in the northeastern basin and the Gulf of Alaska, thus indicating an opposite phase in the low-frequency interannual SST variability between the Alaska gyre and the central North Pacific. Their temporal expansion of that mode pointed to a cooler Alaska gyre SST in the 1970s and a warmer one in the 1980s, as indicated here in Fig. 2a. They also noted that winter SST tendency (SST change from early to late winter) correlations with 500-mb height anomalies favor large-scale atmospheric forcing of the ocean. In the Gulf of Alaska, these correlations indicated a winter SST warming tendency associated with a stronger Aleutian low (+PNA).

3. Data processing and mean fields

The set of 9382 XBT and 2769 STD stations obtained from the National Oceanographic Data Center (see the appendix) were used to compute 0–450 dbar dynamic height, $\eta(x, y, t)$, within the boundaries 50°N latitude, 160°W longitude and the coast. Converting XBT temperature profiles to dynamic height is described by Lagerloef (1994). An rms error of <0.03 dynamic meters (dyn m) was obtained using a regression model relating empirical dynamic height modes to integrated temperature profiles. This empirical halosteric adjustment was a significant improvement over the conventional temperature salinity correlation method in the Alaska gyre. Even with such adjustment, these dynamic heights reflect the integrated heat content of the upper ocean to a large extent, and the linkage with the SST anomalies is anticipated (Fig. 2a). Dynamic heights were then interpolated to a horizontal (1° lat × 1° long) and temporal grid by an objective analysis using decorrelation scales of 200 km and 90 days (the appendix). Figure 1 shows the mean dynamic height relative to 450 dbar reflecting the general cyclonic circulation of the gyre.

Wind stress data were derived from the COADS monthly mean 2 deg × 2 deg pseudostress (WU and WV) product available from the National Center for Atmospheric Research. These were converted to wind stress components τ_x and τ_y by reducing WU and WV to equivalent wind speed terms U, V and $W = (U^2 + V^2)^{1/2}$ and applying the Large and Pond (1981) formulation. The stress components were then interpolated to the time and space grid used for the ocean dynamic height data, and applying additional smoothing of 90-day and 1000-km decorrelation scales. From these, the mean stress, Ekman transport components and Ekman pumping velocity were obtained from standard formulas (Fig. 3).

The Ekman transport (Fig. 3b) reveals a highly divergent field with an origin of flux in the northern part of the gyre. Flux is ~1 Sv southward out of the gyre across the southern boundary at 50°N, associated with the prevailing westerlies. The Ekman pumping velocities W_E (Fig. 3c) are maximum in the northern regions where divergence is concentrated and are comparable to or exceeding published values for equivalent wind stress curl, $\rho f W_E$, in the North Pacific (Large et al. 1991; Chave et al. 1991; Rienecker and Ehert 1988). The area integral of W_E yields a net vertical transport comparable to the net Ekman flux out of the gyre. There is an evident process of localized mean Ekman pumping in the north extracting mass from the interior geostrophic flow and conveying it southward in the surface Ekman flux.

4. Low-frequency variations

Taking the conventional approach to studying interannual variability, data presented henceforth are anomalies from seasonally averaged values. As noted above in Fig. 2a, η EOF1 is an expression of similar interdecadal variability previously identified in SST. This mode (shown on expanded scale in Fig. 4a) is dominated by an ~20-yr period punctuated by shorter multiyear variations. It accounts for 29% of the dynamic height variance, which is concentrated in the northern and eastern portions of the gyre. The η EOF2 (8% variance) reflects a large feature in the north and northwest part of the gyre, the negative phase culminating in the mid- to late 1970s and the positive persisting after mode 1 has declined in the late 1980s (Fig. 4). It should be noted that these fields are considerably smoothed by the filtering effect of EOFs. There is considerable mesoscale variability in the higher modes of these seasonal anomalies, as well as a seasonal cycle, which are not being addressed here. Modes 1 and 2 encompass the primary low-frequency decadal variations that are of interest.

A chronology of these variations is clarified with an overlapping sequence of 4-year mean dynamic topography anomalies in Fig. 5. Throughout the early and mid-1970s a large-scale negative anomaly persisted across the basin with a slow migration from east to north to west. Toward the late 1970s and into the early 1980s a positive anomaly accumulated in the southeast and spread north and westward. By the mid-1980s the positive anomaly dominated the basin much the way the negative anomaly had done a decade before, and toward the late 1980s negative anomalies appeared in the south and east. Thus, the 1970s encompass a cool episode, with low dynamic height and SST, while the 1980s were warm, with large-scale positive dynamic height anomalies. Minimum and maximum conditions are represented by the 4-year means marked by 1976 and 1984, respectively. The sum of these anomalies with the mean dynamic topography illustrates the dif-

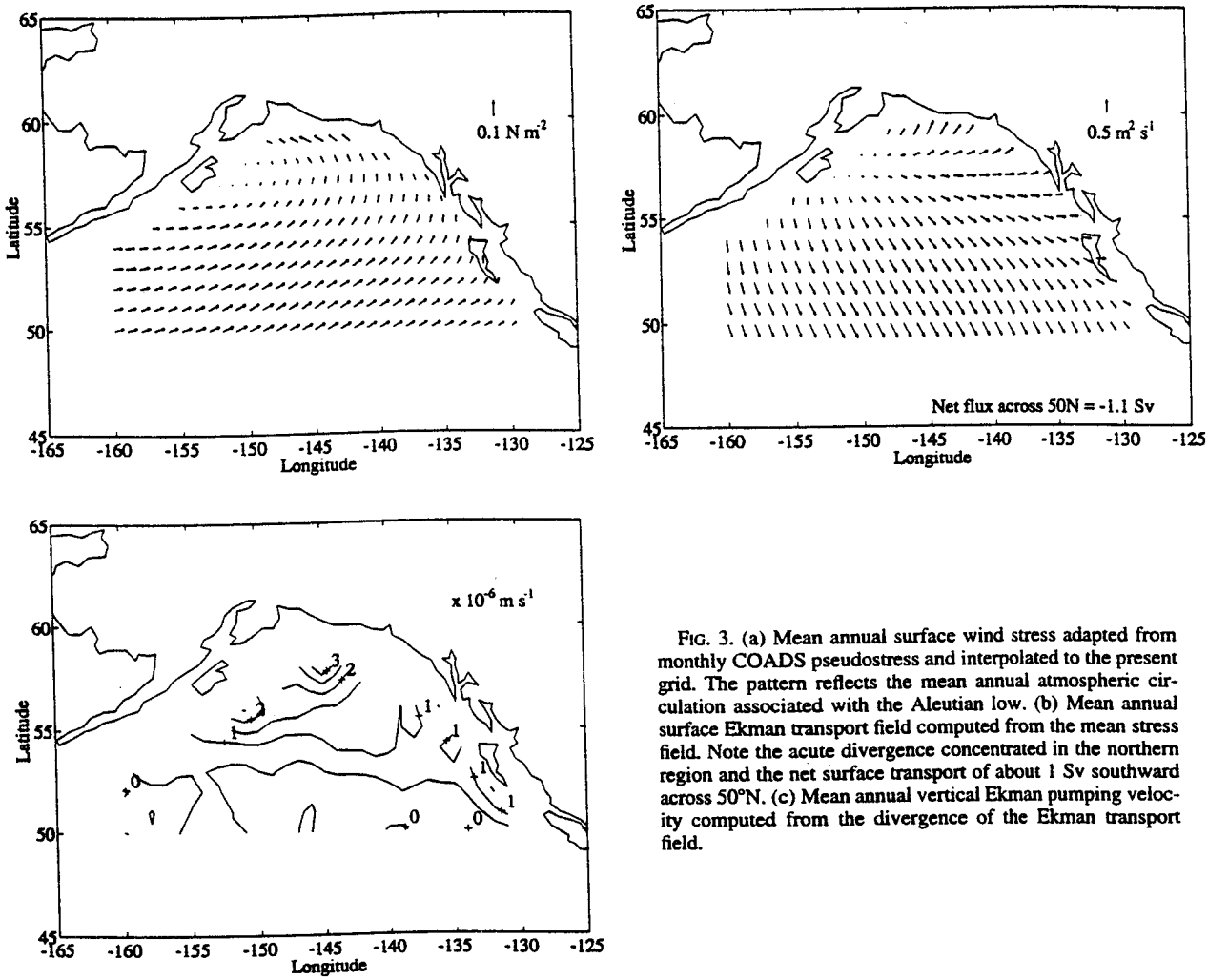

FIG. 3. (a) Mean annual surface wind stress adapted from monthly COADS pseudostress and interpolated to the present grid. The pattern reflects the mean annual atmospheric circulation associated with the Aleutian low. (b) Mean annual surface Ekman transport field computed from the mean stress field. Note the acute divergence concentrated in the northern region and the net surface transport of about 1 Sv southward across 50°N. (c) Mean annual vertical Ekman pumping velocity computed from the divergence of the Ekman transport field.

ferent flow conditions (Fig. 6). In the 4-year mean marked by 1976 the gyre was relatively intense with a well-defined center and strong Alaskan Stream. The period marked by 1984 showed a relatively relaxed circulation and the center displaced southwestward. These changes took place as the Aleutian low pressure system was intensifying between the 1970s and 1980s (Fig. 2b). The ocean data indicate that the gyre filled rather than deepened during this period, counter to the conventional view that the strengthening Aleutian low would spin up the gyre. Warmer conditions in the northeast Gulf of Alaska in conjunction with a stronger Aleutian low are also consistent with patterns seen by Wallace et al. (1990) and others.

The evolving wind stress anomaly field is depicted with a sequence of overlapping 4-year means in Fig. 7 for comparison with Fig. 5. The early to mid-1970s were dominated by north, northwest, and westerly wind anomalies. In the latter decade the wind anomalies shifted to east and southeasterlies as the Aleutian low intensified. Ekman pumping was evidently the primary wind forcing mechanism according to these patterns. Generally a southward and divergent Ekman transport anomaly persisted in the 1970s, with positive W_E inducing upward pycnocline displacement and reduced dynamic height. The converse was true in the 1980s: generally north and east Ekman transport induced convergence and accumulation of warmer buoyant waters in the upper layer. Upwelling anomalies may not entirely account for the SST variations between the decades because a shallow isothermal or inversion layer often exists in the upper halocline of the northern Gulf of Alaska. SST may have been influenced by the surface Ekman transport anomalies, which advected cooler water from the north in the 1970s and warmer water from the south in the 1980s. A canonical correlation analysis (CCA) was applied here to determine modes maximizing the correlation between η and low-pass filtered (two-year running mean) τ, using three EOFs input from each. [See Barnett and Preisendorfer (1987) or Graham et al. (1987) for a description of the analysis.] The τ CCA1 spatial amplitude depicted a

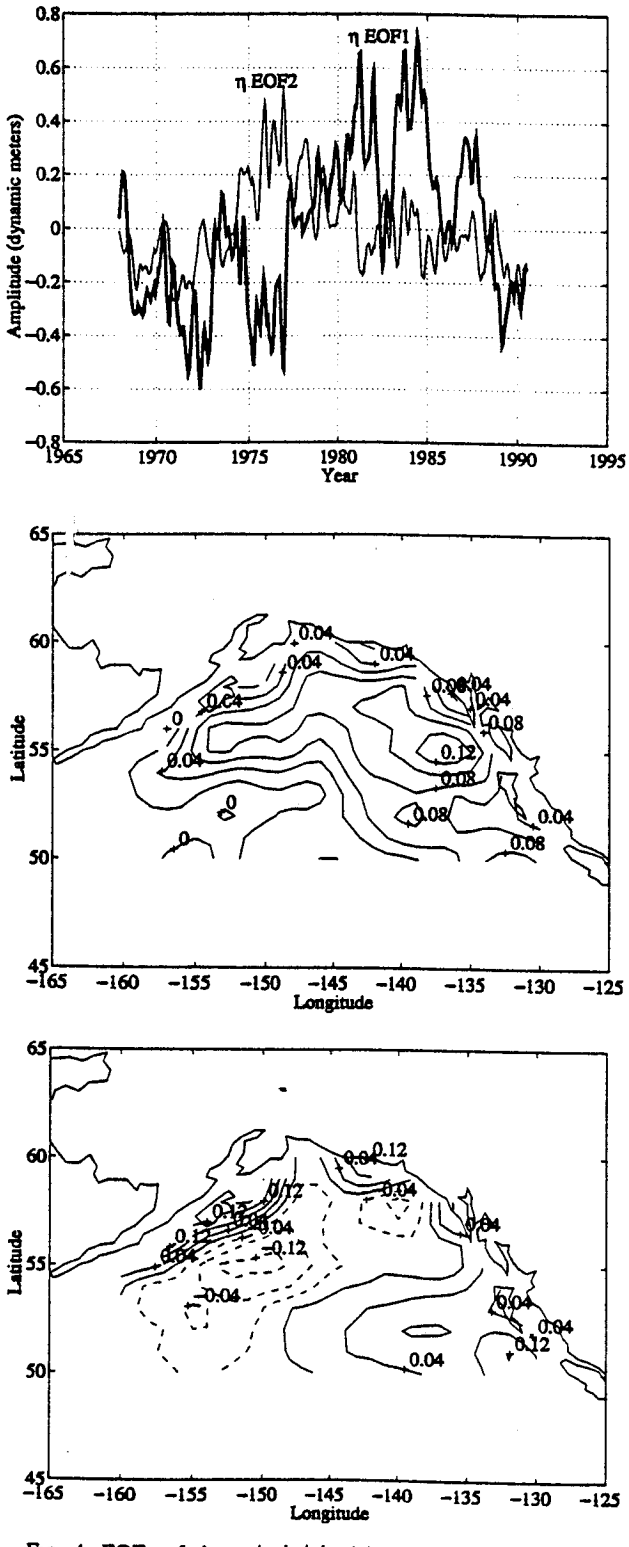

FIG. 4. EOFs of dynamic height (η) anomalies from seasonal means. (a) Time series of η EOF1 (dark) and η EOF2 (light), containing 29% and 8% of the variance, respectively. (b) η EOF1 spatial pattern showing the positive anomaly across the east and north regions of the gyre. (c) η EOF2 spatial pattern showing a major feature in the north and northwest part of the gyre (dashed contours are negative).

NW–SE oriented wind pattern, with a zone of maximum stress and minimal curl dominating the central portion of the gyre, generally clockwise curl to the east and counterclockwise to the west (Fig. 8a). The τ CCA1 and η CCA1 time series amplitudes (Fig. 8b) showed the same negative phase during the 1970s and positive in the 1980s (correlation $r = .69$). The corresponding η CCA1 spatial amplitude (not shown) was nearly identical to η EOF1 (see Fig. 4b).

5. Transient response to stochastic forcing

An inspection of Fig. 8b indicates a slight lag between τ CCA1 and η CCA1 time series, even though they represent signals with the highest in-phase correlation computed by the CCA. The delayed response was examined further with CCA computed at various lags. The η input was limited to EOF1 in this case because it is the dominant signal to be explained and because η EOF2 appears to represent a propagating feature (see section 6) that otherwise influences the lagged CCA in a manner not representing direct forcing. Maximum canonical correlation of $r \approx 0.8$ was found with τ leading η by $\sim$1 year. Secondary peaks with η leading τ by $\sim$3 years ($r \approx 0.7$) and τ leading η by $\sim$4 years ($r \approx 0.58$) are related to an evident 3–4 year variation, which will be the subject of another investigation and not discussed further here. The primary peak at 1-year lag gives a strong indication that the dynamic height variations are a delayed response to wind forcing.

To study this transient response with the Markov model, Eq. (1), it was necessary to compute the Ekman pumping velocity W_E. This was done using a finite-difference estimate of Ekman transport divergence. The wind stress data were unfiltered, except for the 90-day decorrelation scale applied with the objective analysis, and retained an unknown level of spurious measurement noise. To minimize the influence of this error on subsequent estimates of the curl, the stress components τ_x and τ_y were synthesized from their first four EOF modes (89% variance retained) prior to computing the Ekman terms. (The truncation criteria followed the usual practice of retaining modes whose Eigenvalues remained above those from EOFs of white noise.) The resultant W_E anomalies are interpolated to the same grid as the other variables except that points within one grid space of the coast were lost due to the finite differencing.

It is important to briefly discuss the predominant characteristics of the variability. Here W_E EOF1 shows a concentric pattern centered over the gyre, while W_E EOF2 shows broad downwelling across the northeast and upwelling to the west (Fig. 9). In the context of the Ekman pumping hypothesis, the W_E EOF2 rather than the W_E EOF1 pattern is more consistent with the τ CCA1 and η EOF1 patterns. The two-year running mean of the W_E EOF amplitude time series depicts the

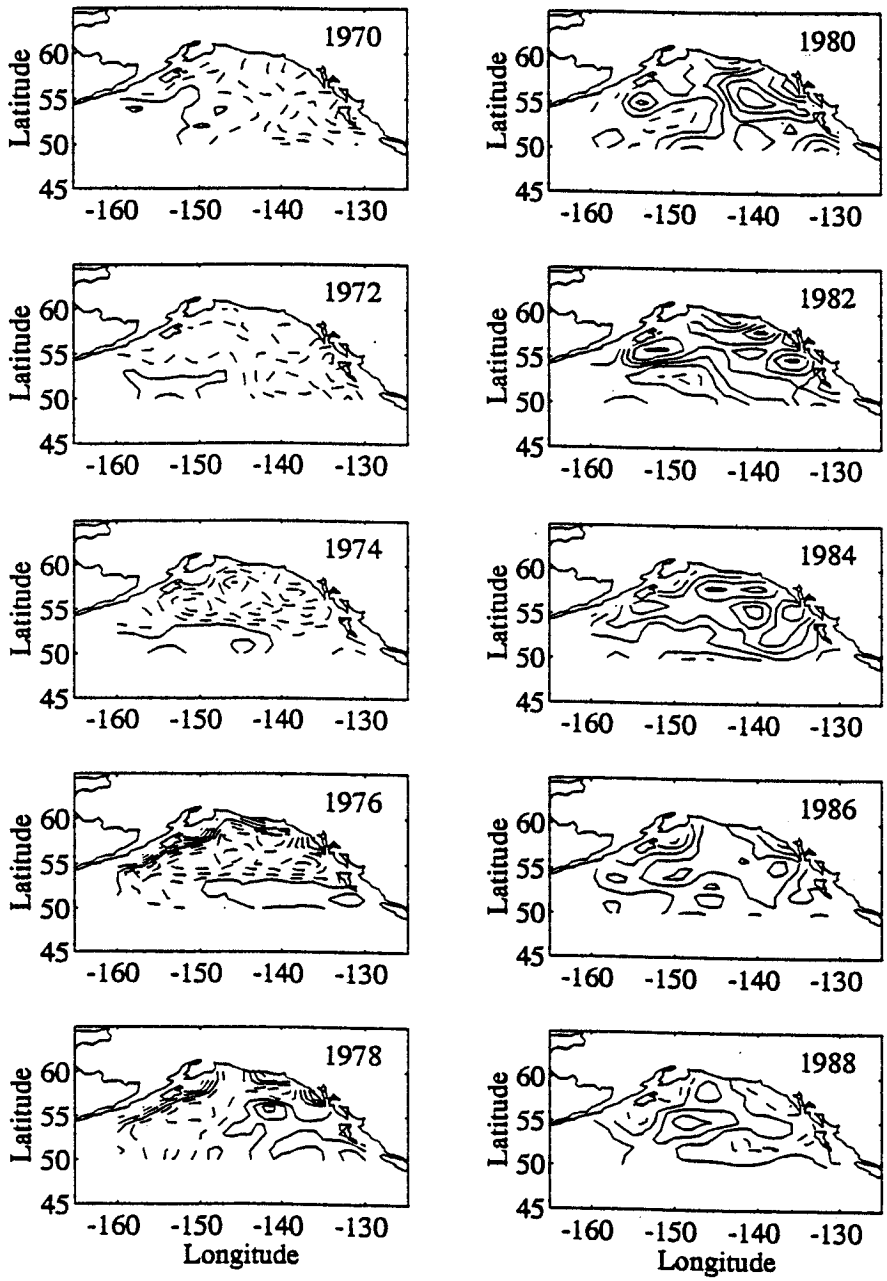

FIG. 5. Sequence of four-year running means of η anomalies centered at the start of the year indicated in each frame (e.g., 1970 represents the average of years 1968, 1968, 1970, 1971). Note the apparent counterclockwise progression of a large-scale negative anomaly around the gyre in the 1970s, followed by the large-scale positive anomaly in the 1980s (dashed contours are negative).

low-frequency components of these modes (Fig. 10). W_E EOF1 displays variations of ~5 yr periods, while W_E EOF2 shows a low-frequency trend similar to the increasing PNA index from the 1970s to the 1980s (cf. Fig. 2b). Thus W_E EOF2 appears to carry much of the subtle low-frequency variability associated with the longer-scale climate variations. In contrast, the unfiltered W_E EOF time series are clearly dominated by much shorter timescales (Fig. 11), where low frequencies have much smaller amplitude than the shorter timescale atmospheric noise. Composite spectra of η and W_E (Fig. 12) demonstrate the redness of oceanic variability compared to the white W_E spectrum. This timescale separation is characteristic of stochastic climate forcing.

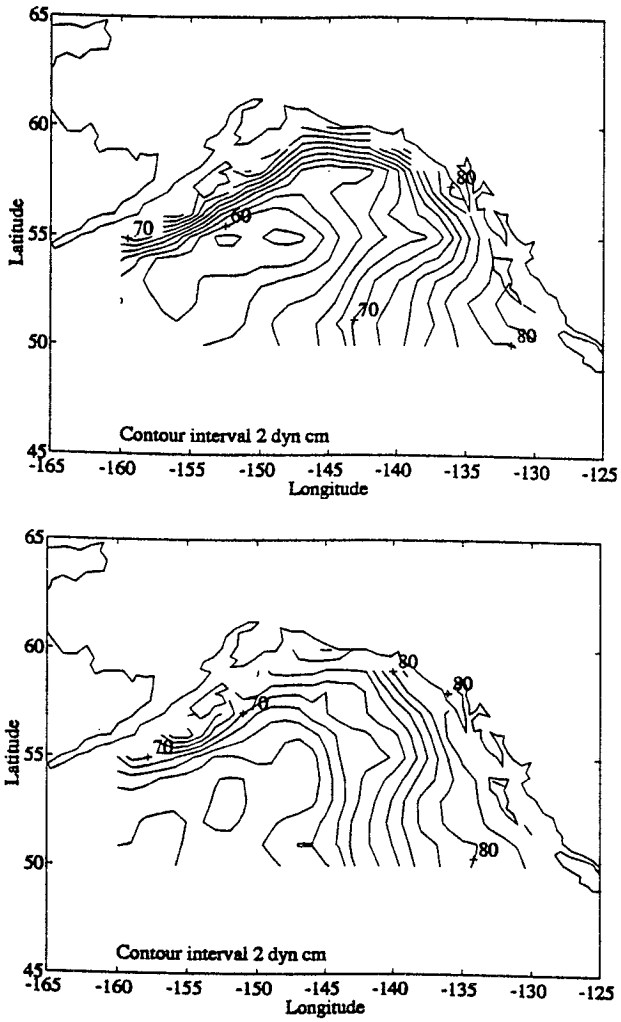

FIG. 6. Four-year mean η anomalies added to the mean annual dynamic height field for the periods marked 1976 and 1984 in Fig. 5. (a) In the four years marked by 1976 the gyre was relatively intensified with a well-defined center and strong Alaskan Stream. (b) The period marked by 1984 showed relatively relaxed circulation and the center displaced southwestward.

Ekman convergence results in a $-W_E$, which should induce a positive $\partial\eta/\partial t$ through pycnocline motion. This implies that the low-frequency variations should be out of phase by $\pi/2$ and η should lag $-W_E$, whereas the CCA analysis above showed a high degree of correlation nearly in-phase. This can be reconciled by examining the stochastic forcing model (1) at each end of the spectrum. At high frequencies $\omega \gg \lambda$,

$$\frac{\partial \eta}{\partial t} \approx -\alpha W_E \tag{2}$$

and the response η is an accumulation of random impulses (random walk); η is theoretically in quadrature with $-W_E$ and the spectral slope is ω^{-2}. At frequencies $\omega \ll \lambda$,

$$\lambda\eta \approx -\alpha W_E, \tag{3}$$

and the response is approximately in phase with $-W_E$. The low-frequency end of the spectrum becomes white and the variance statistically stationary (Hasselmann 1977). The subrange of frequencies $\omega \sim \lambda$ marks the transition from red to white spectra and quadrature to in-phase response. It will be shown below that $\lambda \approx 1\ \text{yr}^{-1}$ in the gyre, with a corresponding period $T \approx 2\pi\lambda^{-1} \approx 6$ yr. Thus the subrange $\omega \sim \lambda$ encompasses the interannual to interdecadal band, which dominates the observed variability. Note that T is about three times larger than the minimum Rossby wave period $T_{\min} \approx 1.9$ yr, which is the high-frequency dynamic limit of the baroclinic response. The effective timescale of the low-pass filtering process by the ocean is defined by $\omega \sim \lambda$. Figure 12 illustrates an idealized frequency spectrum $F(\omega) \propto (\omega^2 + \lambda^2)^{-1}$ (see Frankignoul 1981), with $\lambda = 1\ \text{yr}^{-1}$, superimposed on η. As λ decreases, the transition portion of the spectrum shifts to lower frequencies and the decorrelation timescale of the ocean response increases. It can be shown that the theoretical phase angle between η and W_E in Eq. (1) is $\theta = \tan^{-1}(\omega/\lambda)$, which tends toward zero as $\omega \to 0$. The phase lag in units of time for a given frequency is θ/ω, which asymptotically approaches λ^{-1}, or $\sim$1 yr, as $\omega \to 0$; consistent with the $\sim$1 yr lag CCA given above.

In discrete form, (1) is expressed as

$$\frac{\eta(t+1) - \eta(t)}{dt} = -\alpha W_E(t) - \lambda\eta(t) \tag{4}$$

or

$$\eta(t+1) = \phi\eta(t) - \alpha W_E(t)dt, \tag{5}$$

where $\phi = 1 - \lambda dt$, and $(t+1)$ and (t) indicate discrete time steps separated by dt. When W_E is uncorrelated white noise, this is a simple first-order autoregression (AR1) process (Wei 1990); ϕ is the AR1 coefficient equivalent to the lag 1 autocorrelation coefficient. Ideally, the lag interval dt should be the natural decorrelation timescale for W_E. This is difficult to properly determine here because the original COADS wind data are monthly means and were subsequently smoothed further in the objective analysis (the appendix), where the sample interval was arbitrarily selected ($dt = 1/16$ year) and not prescribed by the natural decorrelation timescale. Estimating ϕ through the autocorrelation function was therefore not satisfactory in this case, and a different approach was taken.

By recursive substitution in (5), it can be shown that η at any time step $(t+1)$ is determined by the summation over N previous time steps:

$$\eta(t+1) = \phi^{N+1}\eta(t-N) - \alpha dt \sum_{n=0}^{N} \phi^n W_E(t-n). \tag{6}$$

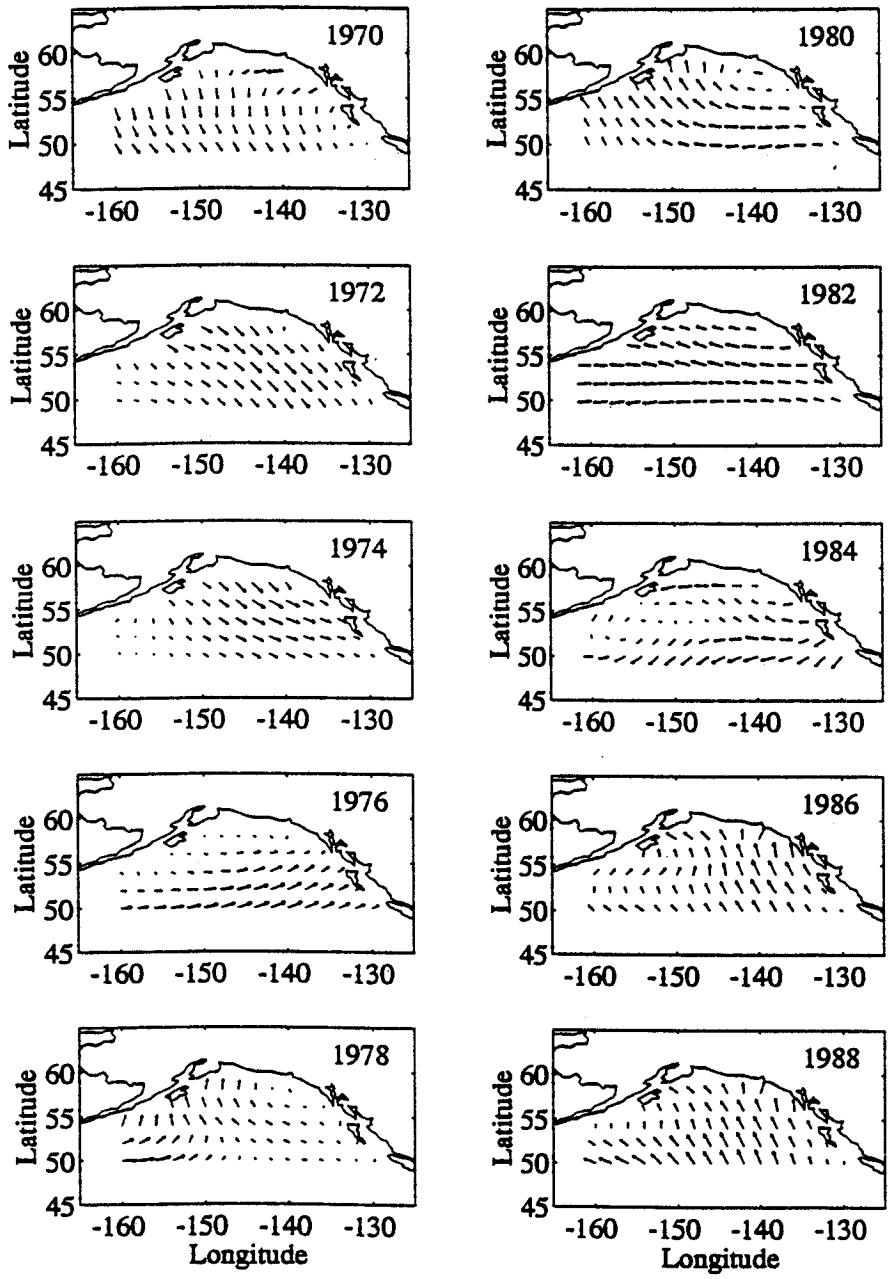

FIG. 7. Sequence of four-year running mean wind stress (τ) anomalies centered at the start of the year indicated in each frame, as in Fig. 5. The early to mid-1970s were dominated by north, northwest, and westerly wind anomalies. In the latter decade the wind anomalies shifted to east and southeasterlies as the Aleutian low intensified.

Note that with $0 < \phi < 1$, the first term on the right vanishes for large N and the function becomes independent of the initial state at $t - N$. In any case, the initial condition $\eta(t - N) = 0$ can be assumed with no loss of generality and the term can be ignored. In the remaining summation terms, α is seen as a scaling coefficient between W_E and η, which simply determines the amplitude of the response function. The weights ϕ^n serve as a filter. For $\phi \to 0$ ($\lambda \to 1/dt$) the weights tail off sharply; the function becomes independent of its history and approaches a likeness of W_E. Conversely, as $\phi \to 1$ ($\lambda \to 0$) the function is highly dependent on its past and approaches an ordinary random walk with inverse square spectral slope.

Coefficients ϕ and α can be estimated from (5) by multiple linear regression in the form $z = \phi x + \alpha y$,

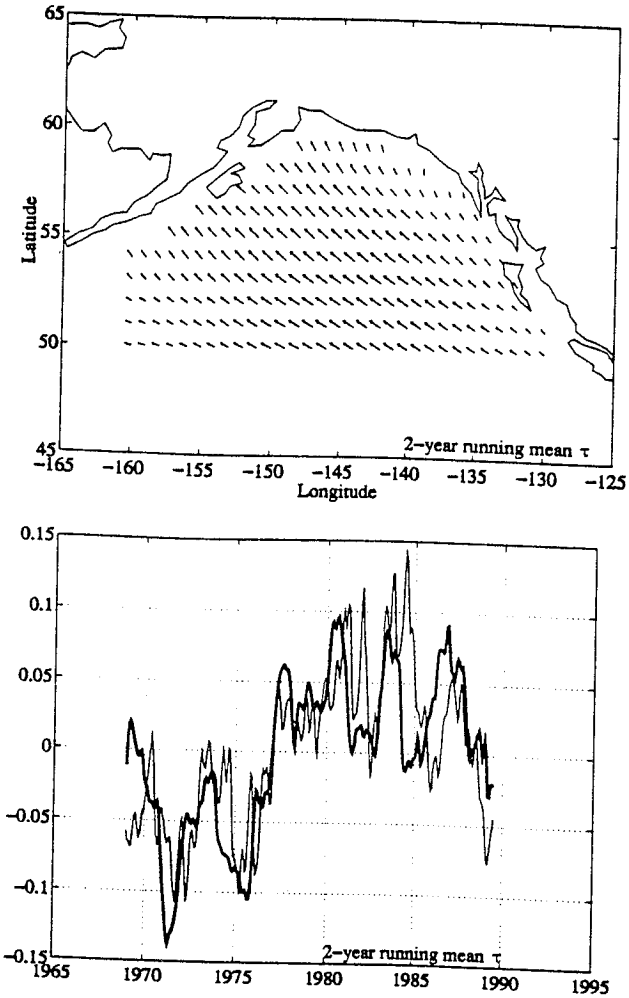

FIG. 8. (a) Spatial pattern for τ CCA1, the first canonical correlation analysis (CCA) mode between τ (two-year running mean) and η. A zone of maximum stress and weak curl dominated the central portion of the gyre, with generally clockwise curl to the east and counterclockwise to the west (in the positive phase). This represents the wind stress anomaly mode pattern having the greatest correlation with η. (b) The time series amplitudes of τ CCA1 (dark) and η CCA1 (light), showing the low anomaly in the 1970s and high in the 1980s as seen in η EOF1.

where $z = \eta(t + 1)$, $x = \eta(t)$ and $y = -W_E(t)dt$. Subsequently applying these in (5) to hindcast η, it became apparent that α was seriously underestimated and ϕ slightly overestimated, owing to the high η autocorrelation and weak η versus W_E cross correlation. An iterative procedure was devised to find the best fit between the observed η and the hindcast computed from W_E, as follows. Step 1: An initial guess of ϕ was taken from the above multiple regression. Step 2: A hindcast estimate η_e was computed with

$$\eta_e(t + 1) = \phi\eta_e(t) - W_E(t)dt, \qquad (7)$$

which is equivalent to (5) except for omitting the scaling coefficient α. Step 3: α was then estimated by linear regression of $\eta = \alpha\eta_e$, which yielded a larger value than the initial multiple regression. Step 4: A new estimate of ϕ was obtained by linear regression of $\{\alpha W_E(t)dt + \eta(t + 1)\} = \phi\eta(t)$. This reduced ϕ slightly as α increased. Steps 2–4 were repeated until the rms difference between η and $\alpha\eta_e$ ceased to change significantly. Resulting values of ϕ ranged from 0.84 to 0.98 with a median of 0.94. The corresponding damping coefficient time scale $\lambda^{-1} = (1 - \phi)/dt$ fell in the range 0.5–2.5 yr with a median value of ~1 yr.

The scaling coefficient α was on the order of 10^{-2}–10^{-3}, or $\sim g'/g$ (where g' is reduced gravity), as would be expected from dynamic scaling arguments. However, the hindcast amplitudes $\alpha\eta_e$ tended to be about a factor of 2 smaller than the observed η time series. From (3), α represents the low-frequency regression between $-W_E$ and $\lambda\eta$. The spatial pattern was found to be nonuniform (Fig. 13), with the region of strongest response concentrated in the eastern half of the gyre. This eastward bias is consistent with η EOF1 and the implicit Ekman pumping in W_E EOF2. A large region enclosed by $\alpha \approx 0$ signifies that the local wind forced response is weak through much of the western part of the gyre. This is the region dominated by W_E EOF1, indicating the ocean did not respond locally to variability in this mode in spite of its being the most energetic (60%). Discussions in section 6 will consider some explanations for this result.

A comparison between the hindcast $\alpha\eta_e$ and the observed η provides an assessment of the Markov model. Recall that $\alpha\eta_e$ is a time series at each grid point estimated solely from W_E and two coefficients, α and either λ or ϕ. The correlation between $\alpha\eta_e$ and η is evaluated with CCA using three EOF modes from each dataset as input. (The EOF1 time series of each were actually quite similar, with a correlation of $r = .73$.) The respective CCA1 time series amplitudes (Fig. 14a) represent the optimal correlation between the two fields. They correspond quite closely with a correlation of $r = .79$. The respective CCA1 spatial amplitude contours are generally aligned and depict similar concentration of variability in the eastern portion of the gyre (Fig. 14b). The η CCA1 pattern is virtually identical to η EOF1, and it is evident that the dominant mode of interdecadal dynamic height variability is largely accounted for with this simple model of direct Ekman pumping. The CCA2 and CCA3 modes (not shown) had much smaller correlations (.41 and .22), and their spatial amplitude patterns did not portray the level of agreement as CCA1 to suggest that local forcing of the same sort was explaining the remaining η variance. Of particular note, $\alpha\eta_e$ did not produce a mode resembling η EOF2, suggesting that an important fraction of the lowest frequency variability was not locally forced.

The nature of the oceanic response to stochastic forcing is further illustrated in Fig. 15 with a simulation in which (4) is integrated over 100 years using computer-generated random white noise for W_E, $\lambda^{-1} = 1$ yr, and

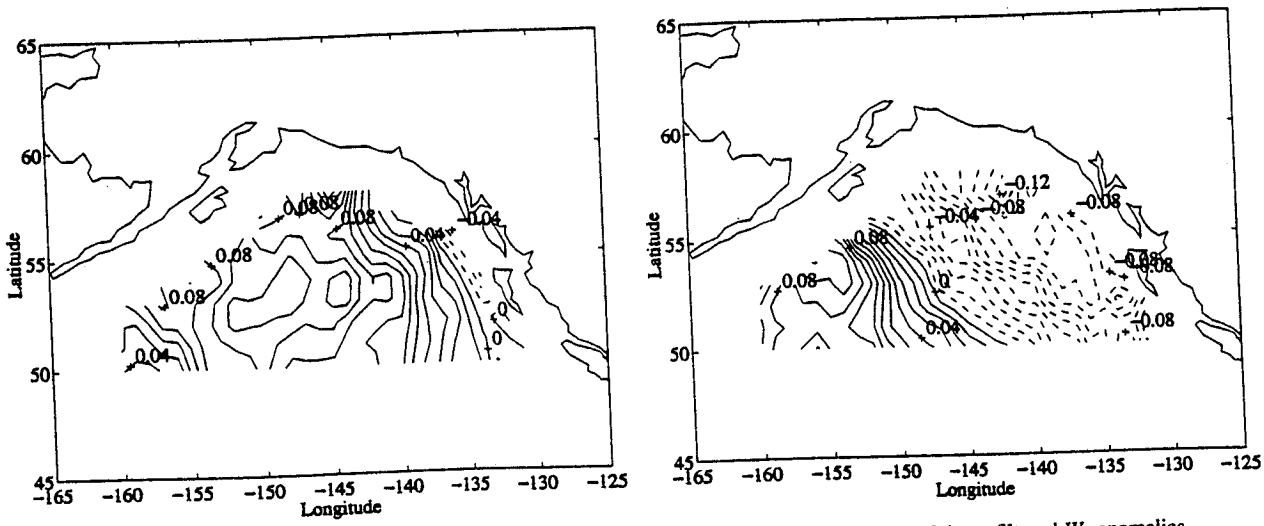

FIG. 9. Spatial patterns for Ekman pumping velocity modes (a) W_E EOF1 and (b) W_E EOF2 of the unfiltered W_E anomalies, containing 60% and 27% of the variance, respectively.

α arbitrarily scaled. Decadal variability arises naturally from the random forcing. The lower half of the figure shows η EOF1 to illustrate that the measured oceanic variability is similar in nature to the artificially forced autoregression model. Note that the time axes were deliberately aligned to highlight the resemblance between the observed dynamic height and a similar segment of the random simulation. The similarity is purely coincidental, and this sequence was chosen for illustration from several such simulations. This provides a means to test the statistical significance of the CCA results. Three random white noise sequences were passed through the autoregression model to generate artificial sequences like any 22.5-year segment of Fig. 15. The EOFs of these were supplied to a CCA with the first three η EOFs, and the CCA1 coefficient was recorded. The process was repeated for 1000 trials to tabulate the CCA1 statistics. Using $\lambda^{-1} = 1$ yr in the autoregression, the largest coefficient was .78, or slightly less than .79 obtained with $\alpha\eta_e$. Using $\lambda^{-1} = 2$ yr, 1.2% of the artificial coefficients exceeded .79. Given that λ^{-1} generally fell between 0.5 and 2 yr with a median of 1 yr, it is concluded that the CCA coefficient between $\alpha\eta_e$ and η is significant at about the 99% confidence level.

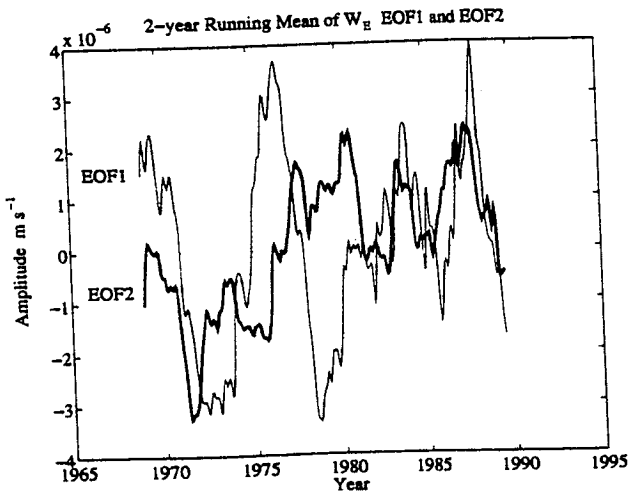

FIG. 10. Two-year running mean filter of W_E EOF1 and W_E EOF2 amplitudes showing that mode 2 reflects the slow variation associated with the increasing PNA index (Fig. 2b).

6. Discussion

The Markov model results remain deficient in some respects. As noted, the low-frequency variability associated with η EOF2 was not reproduced. This anomaly is centered considerably westward of η EOF1 and generally lags by a few years. Referring again to Fig. 5, it is evident that the large-scale anomalies propagated generally westward, and it is common for two EOF modes to depict near quadrature phases of a propagating feature. In this case, it is a likely indication of long Rossby wave radiation from the eastern region of local forcing. Interannual baroclinic Rossby waves have been documented along line P, near the southern boundary of the present study area, by White and Tabata (1987). The conventional reduced gravity equation for a forced long planetary wave in a 1.5-layer ocean, expressed in terms of dynamic height, is (Kelly et al. 1993)

$$\frac{\partial \eta}{\partial t} - L_D^2 \beta \frac{\partial \eta}{\partial x} = -\frac{g'}{g} W_E, \tag{8}$$

where β is the meridional planetary vorticity gradient, g' reduced gravity, and local relative vorticity has been

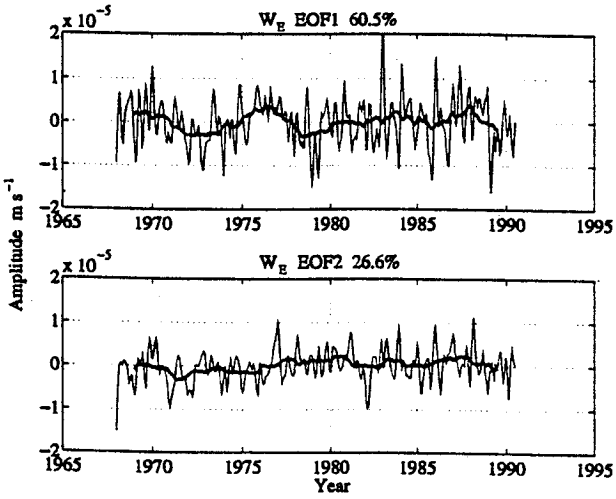

FIG. 11. Unfiltered W_E EOF1 and W_E EOF2 amplitude time series (light curves), which demonstrate the timescale separation between the climatic forcing term W_E and the response term η seen in Fig. 4a. The two-year running means (dark curves) are superimposed (see Fig. 10).

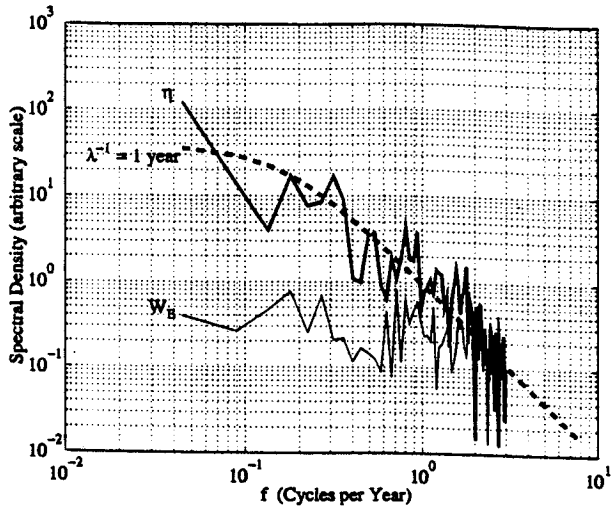

FIG. 12. Composite spectra formed by averaging the spectral density of the lowest three EOF modes of η (dark) and W_E (light) respectively. Dashed curve is the idealized Markov spectrum $(\omega^2 + \lambda^2)^{-1}$ with $\lambda = 1$ yr^{-1} and $\omega = 2\pi f$.

ignored for large-scale $L \gg L_D$. The internal Rossby radius L_D is ~16 km based on the vertical eigenvalue solution to the mean buoyancy profile (see also Emery et al. 1984). The homogeneous solution to (8) is the nondispersive long Rossby wave with a phase speed $C = L_D^2\beta \sim 105$ km yr^{-1} at 55° latitude. The very long period $T \sim 20$ yr characterized by η EOF1 and EOF2 implies a wavelength $L \sim 2000$ km, or about 30° longitude. This is the width of the study area and is consistent with the length scales of the features in these modes. Kelly et al. (1993) solved (8) with an idealized seasonally varying standing wave wind curl pattern to model wind-driven annual Rossby waves in the California Current. The solution contained standing and propagating modes with length scales dictated by the wavenumber of the atmospheric forcing and the free wave dispersion relation respectively. It is likely that similar dynamics are at work here on longer timescales, in particular the excitation of a long free wave with a wavelength determined by the timescale of the forcing and the dispersion relation rather than by the length scale of the forcing. The atmospheric wavelength associated with the Aleutian Low exceeds 5000 km, so the system is not near resonance. A major discrepancy between the observations presented here and Kelly's solution is that the standing wave response is out of phase with the forcing in the latter result. The low-frequency in-phase response shown here is explained by the damping term in (3). This suggests that a more general theory should include both damping and Rossby wave dynamics. Noting the similarity between (1) and (8), this can be expressed as

$$\frac{\partial \eta}{\partial t} - L_D^2\beta\frac{\partial \eta}{\partial x} = -\alpha W_E - \lambda\eta, \qquad (9)$$

where the damping embodies higher-order terms, which were ignored in the simplification of (8) from momentum and mass conservation equations. It is beyond the scope of this work to attempt a rigorous derivation of such terms, but the empirical results provide numerical constraints, which may be useful in determining appropriate scales.

Another discrepancy with the Markov model results is the unbalanced oceanic response to the first two W_E EOFs. As noted, W_E EOF1 has a pattern centered over the gyre and has greater variance both in the higher and

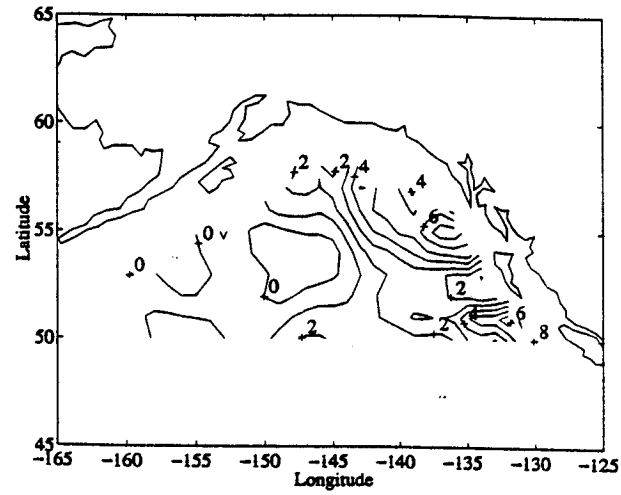

FIG. 13. Contours of the amplitude coefficient α derived from the Markov autoregression model. Note the eastward bias indicating dominant Ekman pumping response in the eastern region and weak response ($\alpha \sim 0$) in the western portion.

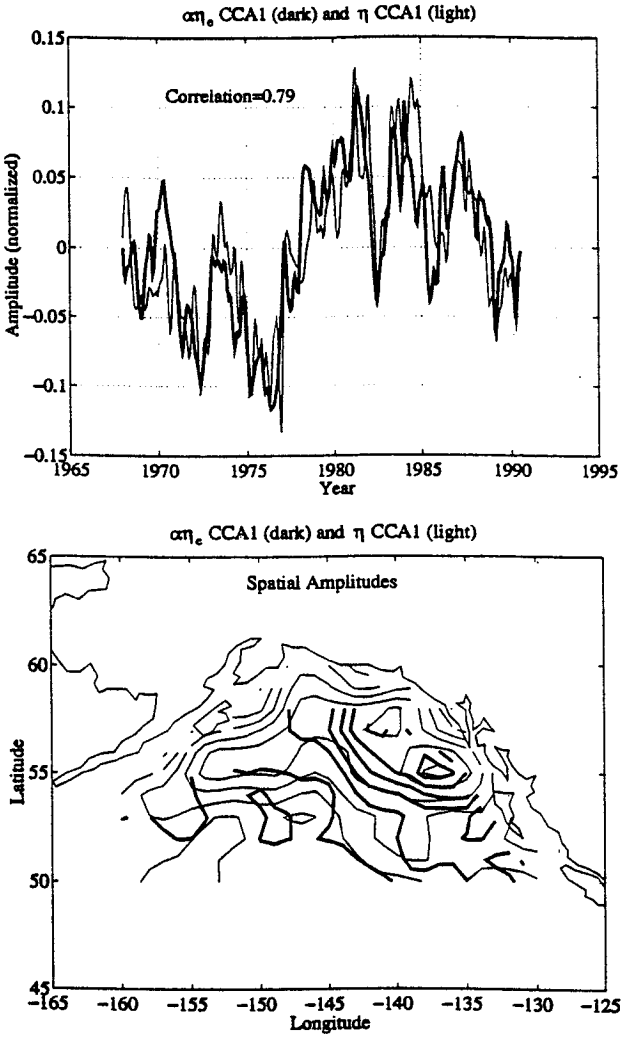

FIG. 14. Canonical correlation analysis results between the observed dynamic height field η and that estimated η_e from the observed Ekman pumping W_E using the Markov stochastic forcing model to hindcast. (a) Temporal amplitudes η CCA1 (light) and $\alpha\eta_e$ CCA1 (dark) with a canonical correlation of 0.79. The major events on 5–20-yr timescales are clearly replicated in both signals. (b) Spatial amplitude contours of η CCA1 (light) and $\alpha\eta_e$ CCA1 (dark). The general agreement signifies that the CCA1 time series share a similar spatial pattern of amplitudes between the observed and hindcast fields, particularly in the eastern portion.

lower frequencies. Yet, there is little evidence of direct local response in accordance with the stochastic model. For some reason that is not clear, the ocean appears to have been more resonant with the spatial and temporal pattern associated with W_E EOF2, which brought more vigorous Ekman pumping in the east and less in the center of the gyre. It is possible that the local midgyre response was obscured by the long propagating wave postulated above. An anonymous reviewer suggested that the observed response may be influenced by the eastern boundary current, bottom topography, or variability associated with the Sitka eddy (Tabata 1982). Also, other forcing mechanisms such as surface heat flux may be important. The mean annual heat flux is near zero in the eastern part of the gyre and increases in magnitude toward the west according to new estimates by Tziperman and Bryan (1993). A recent paper by Jacobs et al. (1994) describes a very long crested, long-lived Rossby wave propagating northwestward across the North Pacific subsequent to the 1982–83 El Niño. The northeastern extremity of the wave appears to have extended into the Gulf of Alaska according to GCM simulations, indicating a remotely forced oceanic teleconnection which may influence the dynamic topography on these timescales.

To this point little has been said regarding the Sverdrup transport. A barotropic Sverdrup balance has been described in deep North Pacific currents on shorter than yearly timescales (Koblinsky et al. 1989; Niiler and Koblinsky 1985). Regarding the baroclinic mode, it is commonly accepted that a quasi-steady Sverdrup balance will account for the interannual large-scale variations in the meridional transport and the Alaskan Stream. It was noted above, however, that prior observations do not support this on seasonal to interannual timescales. Wunsch and Roemmich (1985) also questioned the basic premise in the subtropical North Atlantic. In the quasi-steady version of (8), a negative W_E anomaly pattern over the eastern portion should correlate with decreased $\partial\eta/\partial x$. This implies an η anomaly with a relative high at the gyre center and low

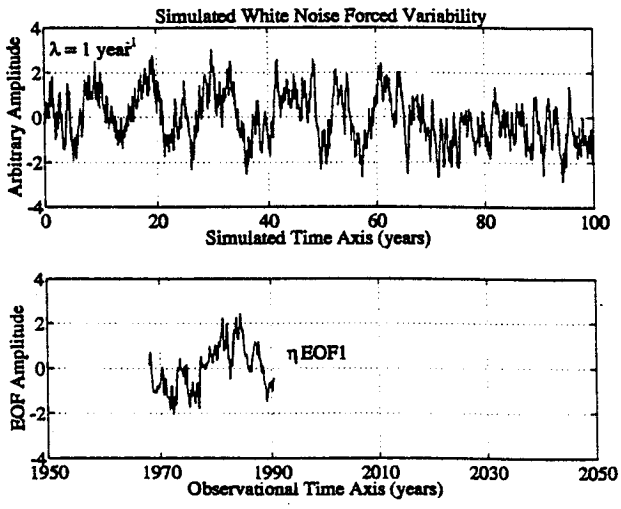

FIG. 15. A simulation of stochastically forced variability using the Markov model [Eq. (4)] with computer-generated white noise for W_E and $\lambda = 1\ \text{yr}^{-1}$ (top panel). The low-frequency variations produced are similar in nature to observed η variability, as demonstrated with η EOF1 (bottom panel). Note that the time axes were deliberately aligned to highlight the similarity between the observed dynamic height and a segment of the random simulation. The similarity is purely coincidental, and this sequence was chosen for illustration from several such simulations.

at the eastern boundary rather than the observed pattern. To consider whether the quasi-steady assumption is valid, note that the terms on the left side of (8) are similar in magnitude for decadal timescales of $T = L\beta^{-1}L_D^{-2} \approx 10-20$ yr (with $L \approx 1000-2000$ km). This is the period of the long Rossby wave that would bring about the geostrophic adjustment to a large-scale change in the wind curl. Quasi-steady Sverdrup balance would require the wind timescale to be many decades before the first term in Eq. (8) becomes negligible. This slow adjustment was also described by Liu (1993) with an ideal two-layer subtropical gyre model response to a single step change in Ekman pumping. The timescale required for Sverdrup adjustment remains much longer than the duration of this 22.5-year record. Consequently, it should be no surprise that the baroclinic response seen here is not consistent with theoretical Sverdrup transport. The transient response is a local Ekman pumping effect to which the meridional flow adjusts geostrophically rather than responding directly to the wind curl in Sverdrup balance.

Randomly forced decadal variability as seen in Fig. 15 will obscure the signature of weak 18.6 year nodal tide SST variation posed by Royer (1993), necessitating very long and stable records to verify the harmonic constituent. Royer reviewed several examples of ~18–22 year variability in climate indices in North America, the North Atlantic, in various fish stocks, and other cases. A significant spectral peak in this band for the Sitka, Alaska, coastal air temperatures, which are coherent with adjacent SST, strengthened the argument in favor of the nodal tide. However, it remains unresolved whether this variability originates in the ocean (i.e., the nodal tide) or in the atmosphere. The results here demonstrate that low-frequency periodicity in the atmospheric circulation would be transferred to the ocean and suggests that the stochastic forcing alone accounts for the observed ocean variability.

It has been noted that the climate changes in the North Pacific during this period included deepening of the Aleutian low, southward displacement of Pacific storm tracks, lower SST, and a deeper mixed layer across the central North Pacific and higher SST along the North American coast and Alaska. These are all consistent with the observations presented here. The cause of this large-scale interdecadal anomaly appears to be related to tropical Pacific SST (Graham et al. 1994). However, the point to be made here is that climatic variability witnessed in the Alaska Gyre is clearly a manifestation of much larger scale happenings in the North Pacific ocean–atmosphere climate interactions. Trenberth and Hurrell (1994) presented the large-scale average NP pressure index as a robust gauge of this climatic signal. A smoothed contour plot by year and month (their Fig. 2) shows an interdecadal oscillation of midwinter SLP with minima in the mid-1920s, early 1940s, early 1960s, and mid-1980s. These coincide almost precisely with the peak Alaska coastal air temperatures shown by Royer (1989, his Fig. 8), suggesting these air temperatures are the result of warm air advection by southerly wind anomalies associated with the Aleutian low. This bears on the discussion of the nodal tide above and lends added support to the hypothesis that the interdecadal variations in the Gulf of Alaska are related to the large-scale variations in atmospheric circulation.

7. Summary and conclusions

Circulation in the Alaska gyre is shown to have large-scale variations over decadal timescales during the period 1968–1990. These are related to previously documented interdecadal SST variations, with warmer SST associated with increasing dynamic height in the north and eastern parts of the gyre. The gyre center was farther east and circulation appeared stronger during the cooler SST decade of the 1970s than the warmer SST decade of the 1980s. The Aleutian low (PNA index) intensified during the interim, and the associated wind stress anomalies forced a slowly varying dynamic height anomaly across the northern and eastern part of the gyre through Ekman convergence. This had the effect of displacing the gyre's low somewhat to the WSW, with an apparent relaxation of circulation in the central and eastern gyre in the 1980s rather than a gyre spinup as might be anticipated with the intensified Aleutian low. Reed (1984) had suggested that accumulated pycnocline displacement associated with local wind stress curl accounted for the apparent westward displacement of baroclinic flow observed between two surveys in the early 1980s, and the present results support that hypothesis. The relationship between patterns of wind stress and the dynamic height were not consistent with poleward transport response according to the Sverdrup balance. The data instead support dynamic height response through vertical pycnocline forcing by Ekman pumping and circulation changes by geostrophic adjustment.

The wind curl spectrum was white at periods > 100 days. The transient baroclinic ocean response had a damping timescale of ~1 yr. By approximating the forced climatic response in terms of a first-order Markov autoregression process, the development of decadal-scale variations was explained as the low-frequency oceanic response to stochastic wind forcing. Using this model with observed winds, hindcast dynamic height temporal and spatial variations were consistent with those observed. A simulation using artificial white noise forcing shows the evolution decadal variations similar in nature to the observed variations. These results demonstrate that much of the observed dynamic height and SST interdecadal variability can be attributed to stochastic wind forcing.

Acknowledgments. This work was sponsored by the Office of Naval Research and the National Aeronautics

and Space Administration under Contracts N00014-90-C-0242 and NASW-4824. Oceanographic data were provided by the NOAA National Oceanographic Data Center on CD-ROM NODC-03 *Global Ocean Temperature and Salinity Profiles, Vol. 2 Pacific Ocean.* The COADS pseudostress data were obtained from the National Center for Atmospheric Research. D. Cayan, Scripps Institution of Oceanography, provided access to the 5 deg × 5 deg monthly mean SST data for the North Pacific; M. Wallace, University of Washington, furnished the monthly mean PNA time series; and K. Trenberth, NCAR, provided the NP time series. The efforts of all who contributed to the availability of these datasets is gratefully acknowledged.

APPENDIX

Data Distribution and Objective Analysis

The geographic distribution of observations used in the dynamic height analysis is shown in Figs. A1 and A2. These consist of 9382 XBTs and 2769 STD/Nansen casts, for a total of 12 151 profiles in the study area spanning the time period from 1968 to mid-1990. The latter consist of traditional hydrocasts using sample bottles and reversing thermometers as well as the modern CTD profiles. The method for estimating dynamic height from XBT data is given by Lagerloef (1994). The point observations of 0–450 dbar dynamic height η were interpolated to a fixed grid at the intersection of each whole degree of latitude and longitude. Note that this scale does not resolve the details of the shelf and coast; thus contours may appear at times to cross the shelf and the superimposed shoreline as an artifact of the coarse grid. Only oceanographic station depths extending to >450 m were used in the analysis, so data remain representative of oceanic and not shelf measurements. The temporal resolution of the interpolated fields was set at 16 samples per year so that the Nyquist frequency would be sufficiently high to resolve annual and semiannual signals should they be of interest.

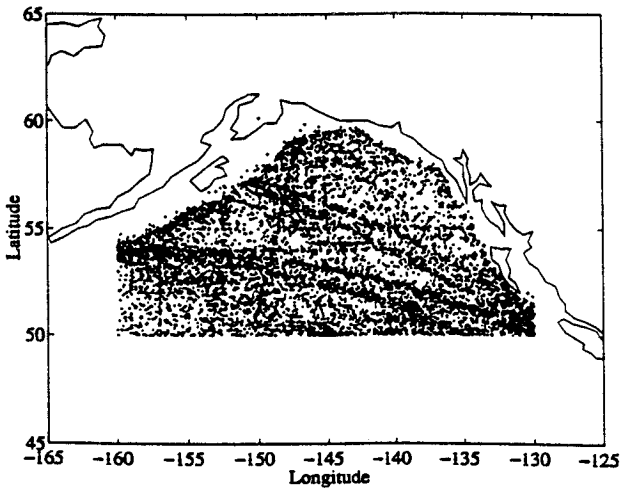

FIG. A1. Geographic distribution of the 9382 XBT stations, 1968 to mid-1990.

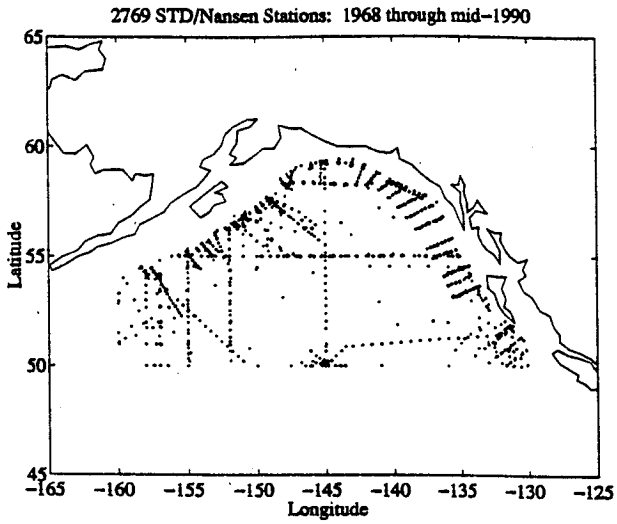

FIG. A2. Geographic distribution of the 2769 STD/Nansen stations, 1968 to mid-1990.

The interpolation followed common practices in statistical objective analysis (e.g., Thiebaux and Pedder 1987). This required the specification of a correlation model, and a simple Gaussian form was used:

$$\sigma = \exp\left[-\left(\frac{\Delta x}{S_x}\right)^2 - \left(\frac{\Delta y}{S_y}\right)^2 - \left(\frac{\Delta t}{S_t}\right)^2\right], \quad \text{(A1)}$$

where Δx, Δy, and Δt are separations in the east, north, and time dimensions, respectively; and S_x, S_y, S_t are the respective decorrelation scales. The mean field was estimated by first taking the ensemble mean of all observations as a first guess and subtracting it from each observation. The interpolation of the residuals was made to each grid point using only the first two terms of (A1) with large scales $S_x = 30°$ longitude and $S_y = 10°$ latitude to ensure a smooth field. Adding back the ensemble mean gave the gridded mean field shown in Fig. 1. The space–time objective analysis began with an interpolation of the mean field to each observing location and subtraction to yield the residual from the local mean at that location. The residuals were then interpolated to the space–time grid using scales $S_x = S_y = 200$ km and $S_t = 0.25$ yr to produce the dataset for subsequent analysis. In order to avoid the inversion of very large correlation matrices, an influence radius was employed to screen observations outside the neighborhood of the interpolation grid point. For computing the mean field, this was arbitrarily set to $r = [r_x^2 + r_y^2]^{1/2}$ with $r_x = r_y = 100$ km. For the subsequent space–time interpolation, $r = [r_x^2 + r_y^2 + r_t^2]^{1/2}$ with $r_x = r_y = 300$ km and $r_t = 0.375$ yr. These radius components were

1.5 times their respective decorrelation scales, so that observations with a correlations less than about $\exp[-(1.5)^2] \sim 0.1$ were ignored. In general, the number of observations included in each interpolation point ranged between about 50 and 200. Interpolation of the 2 deg × 2 deg monthly COADS wind stress was computed with scales $S_x = S_y = 1000$ km and $S_t = 0.25$ years to filter the higher wavenumber errors and reduce noise in the subsequent finite-difference computation of the wind curl. The coarse 2 deg × 2 deg COADS grid implies that the coastal winds and the related coastal Ekman convergence are not well resolved.

REFERENCES

Barnett, T. P., and R. Preisendorfer, 1987: Origins and levels of monthly and seasonal forecast skill for United States surface air temperatures determined by canonical correlation analysis. *Mon. Wea. Rev.*, **115**, 1825–1850.

Bhaskaran, S., G. S. E. Lagerloef, G. H. Born, W. J. Emery, and R. R. Leben, 1993: Variability in the Gulf of Alaska from GEOSAT altimetry data. *J. Geophys. Res.*, **98**, 16 311–16 330.

Brink, K. H., 1989: Evidence for wind-driven current fluctuations in the western North Atlantic. *J. Geophys. Res.*, **94**, 2029–2044.

Chave, A. D., D. S. Luther, and J. H. Filloux, 1991: Variability of the wind stress curl over the North Pacific: Implications for the oceanic response. *J. Geophys. Res.*, **96**, 18 361–18 379.

Cummins, P. F., 1991: The barotropic response of the subpolar North Pacific to stochastic wind forcing. *J. Geophys. Res.*, **96**, 8869–8880.

——, and H. J. Freeland, 1993: Observations and modeling of wind-driven currents in the northeast Pacific. *J. Phys. Oceanogr.*, **23**, 488–502.

Dodimead, A. J., F. Favorite, and T. Hirano, 1963: Salmon of the North Pacific Ocean, Part II: Review of oceanography of the subarctic Pacific region. *Int. N. Pac. Fish. Comm. Bull.*, **13**, 195 pp.

Emery, W. J., W. G. Lee, and L. Magaard, 1984: Geographic and seasonal distributions of Brunt-Väisälä frequency and Rossby radii in the North Pacific and North Atlantic. *J. Phys. Oceanogr.*, **14**, 294–317.

Frankignoul, C., 1981: Low-frequency temperature fluctuations off Bermuda. *J. Geophys. Res.*, **86**, 6522–6528.

——, and K. Hasselmann, 1977: Stochastic climate models, Part II: Application to sea-surface temperature anomalies and thermocline variability. *Tellus*, **29**, 289–305.

——, and P. Müller, 1979: Quasi-geostrophic response of an infinite β-plane ocean to stochastic forcing by the atmosphere. *J. Phys. Oceanogr.*, **9**, 104–127.

——, and R. W. Reynolds, 1983: Testing a dynamical model for mid-latitude sea surface temperature anomalies. *J. Phys. Oceanogr.*, **13**, 1131–1145.

Graham, N. E., J. Michaelsen, and T. P. Barnett, 1987: An investigation of the El Niño–Southern oscillation cycle with statistical models 1. Predictor Field Characteristics. *J. Geophys. Res.*, **92**, 14 251–14 270.

——, T. P. Barnett, R. Wilde, M. Ponater, and S. Schubert, 1994: On the roles of tropical and midlatitude SSTs in forcing interannual to interdecadal variability in the winter northern hemisphere circulation. *J. Climate*, **7**, 1416–1441.

Hasselmann, K., 1977: Stochastic climate models, Part I: Theory. *Tellus*, **28**, 473–484.

Jacobs, G., H. Hurlburt, J. Kindle, E. Metzger, J. Mitchell, W. Teague, and A. Wallcraft, 1994: Decade-scale trans-Pacific propagation and warming effects of an El Niño warming anomaly. *Nature*, **370**, 360–363.

Kelly, K. A., M. J. Caruso, and J. A. Austin, 1993: Wind-forced variations in sea surface height in the Northeast Pacific Ocean. *J. Phys. Oceanogr.*, **23**, 2392–2411.

Koblinsky, C. J., P. P. Niiler, and W. J. Schmitz Jr., 1989: Observations of wind-forced deep ocean currents in the North Pacific. *J. Geophys. Res.*, **94**, 10 773–10 790.

——, P. Gaspar, and G. Lagerloef, 1992: The Future of Spaceborne Altimetry: Oceans and Climate Change. Joint Oceanographic Institutions, 75 pp.

Kushnir, Y., 1994: Interdecadal variations in North Atlantic sea surface temperature and associated atmospheric conditions. *J. Climate*, **7**, 141–157.

Lagerloef, G., 1994: An alternate method for estimating dynamic height from XBT profiles using empirical vertical modes. *J. Phys. Oceanogr.*, **24**, 205–213.

Large, W. G., and S. Pond, 1981: Open ocean momentum flux measurements in moderate to strong winds. *J. Phys. Oceanogr.*, **11**, 324–336.

——, W. R. Holland, and J. C. Evans, 1991: Quasi-geostrophic ocean response to real wind forcing: The effects of temporal smoothing. *J. Phys. Oceanogr.*, **21**, 998–1017.

Levitus, S., 1989: Interpentadal variability of temperature and salinity at intermediate depths of the North Atlantic Ocean, 1970–1974 versus 1955–1959. *J. Geophys. Res.*, **94**, 6091–6131.

Liu, Z., 1993: Thermocline forced by varying ekman pumping. Part I: Spinup and spindown. *J. Phys. Oceanogr.*, **23**, 2505–2522.

Miller, A., D. Cayan, T. Barnett, N. Graham, and J. Oberhuber, 1994: Interdecadal variability of the Pacific Ocean: Model response to observed heat flux and wind stress anomalies. *Climate Dyn.*, **9**, 287–302.

Müller, P., and C. Frankignoul, 1981: Direct atmospheric forcing of geostrophic eddies. *J. Phys. Oceanogr.*, **11**, 287–308.

Musgrave, D. L., T. J. Weingartner, and T. C. Royer, 1992: Circulation and hydrography in the northwestern Gulf of Alaska. *Deep-Sea Res.*, **39**, 1499–1519.

Niiler, P. P., and C. J. Koblinsky, 1985: A local time-dependent sverdrup balance in the eastern North Pacific Ocean. *Science*, **229**, 754–756.

Reed, R. K., 1984: Flow of the Alaskan Stream and its variations. *Deep-Sea Res.*, **31**, 369–386.

——, R. D. Muench, and J. D. Schumacher, 1980: On baroclinic transport of the Alaskan Stream near Kodiak Island. *Deep-Sea Res.*, **27A**, 509–523.

Rienecker, M. M., and L. L. Ehert, 1988: Wind stress curl variability over the North Pacific from the comprehensive ocean–atmosphere data set. *J. Geophys. Res.*, **93**, 5069–5077.

Royer, T. C., 1981: Baroclinic transport in the Gulf of Alaska. Part I: Seasonal variations of the Alaska current. *J. Mar. Res.*, **39**, 239–250.

——, 1989: Upper ocean temperature variability in the northeast Pacific Ocean: Is it an indicator of global warming?. *J. Geophys. Res.*, **94**, 18 175–18 184.

——, 1993: High-latitude oceanic variability associated with the 18.6-year nodal tide. *J. Geophys. Res.*, **98**, 4639–4644.

——, and W. J. Emery, 1987: Circulation in the Gulf of Alaska, 1981. *Deep-Sea Res.*, **34**, 1361–1377.

Samelson, R. M., 1989: Stochastically forced current fluctuations in vertical shear over topography. *J. Geophys. Res.*, **94**, 8207–8215.

——, 1990: Evidence for wind-driven current fluctuations in the eastern North Atlantic. *J. Geophys. Res.*, **95**, 11 359–11 368.

Tabata, S., 1982: The anticyclonic baroclinic eddy of Sitka, Alaska, in the Northeast Pacific Ocean. *J. Phys. Oceanogr.*, **12**, 1260–1282.

Thiebaux, H. J., and M. A. Pedder, 1987: *Spatial Objective Analysis.* Academic Press, 299 pp.

Treguier, A. M., and B. L. Hua, 1987: Oceanic quasi-geostrophic turbulence forced by stochastic wind fluctuations. *J. Geophys. Res.*, **17**, 397–411.

Trenberth, K. E., 1990: Recent observed interdecadal climate changes in the northern hemisphere. *Bull. Amer. Meteor. Soc.*, **71**, 988–993.

——, and J. W. Hurrell, 1994: Decadal atmosphere-ocean variations in the Pacific. *Climate Dyn.*, **9**, 303–319.

Tziperman, E., and K. Bryan, 1993: Estimating global air–sea fluxes from surface properties and from climatological flux data using an oceanic general circulation model. *J. Geophys. Res.*, **98**, 22 629–22 644.

Van Scoy, K. A., D. B. Olson, and R. A. Fine, 1991: Ventilation of North Pacific intermediate waters: The role of the Alaskan Gyre. *J. Geophys. Res.*, **96**, 16 801–16 810.

Wallace, J. M., and D. Gutzler, 1981: Teleconnections in the geopotential height field during the Northern Hemisphere winter. *Mon. Wea. Rev.*, **109**, 784–812.

——, C. Smith, and Q. Jiang, 1990: Spatial patterns of atmosphere–ocean interaction in the northern winter. *J. Climate*, **3**, 990–998.

Wei, W. W. S., 1990: *Time Series Analysis.* Addison-Wesley, 478 pp.

White, W. B., and S. Tabata, 1987: Interannual westward-propagating baroclinic long-wave activity on line P in the eastern midlatitude North Pacific. *J. Phys. Oceanogr.*, **17**, 385–396.

Wunsch, C., 1992: Decade-to-century changes in the ocean circulation. *Oceanography*, **5**, 99–106.

——, and D. Roemmich, 1985: Is the North Atlantic in Sverdrup balance? *J. Phys. Oceanogr.*, **15**, 1876–1880.